ARTICLES
https://doi.org/10.1038/s41563-020-0661-4
nature materials

Dipolar interactions between localized interlayer excitons in van der Waals heterostructures

Weijie Li[1,2], Xin Lu[1,2], Sudipta Dubey[1], Luka Devenica[1] and Ajit Srivastava[1]✉

Although photons in free space barely interact, matter can mediate interactions between them resulting in optical nonlinearities. Such interactions at the single-quantum level result in an on-site photon repulsion, crucial for photon-based quantum information processing and for realizing strongly interacting many-body states of light. Here, we report repulsive dipole–dipole interactions between electric field-tuneable, localized interlayer excitons in the $MoSe_2/WSe_2$ heterobilayer. The presence of a single, localized exciton with an out-of-plane, non-oscillating dipole moment increases the energy of the second excitation by ~2 meV—an order of magnitude larger than the emission linewidth and corresponding to an inter-dipole distance of ~7 nm. At higher excitation power, multi-exciton complexes appear at systematically higher energies. The magnetic field dependence of the emission polarization is consistent with the spin-valley singlet nature of the dipolar molecular state. Our finding represents a step towards the creation of excitonic few- and many-body states such as dipolar crystals with spin-valley spinor in van der Waals heterostructures.

Optical response in atomically thin layered semiconductors is determined by excitons and other excitonic complexes, such as trions and biexcitons that are strongly bound due to increased Coulomb interactions in the truly two-dimensional (2D) limit[1,2]. In addition, due to the type-II band alignment in heterobilayer of $MoSe_2/WSe_2$, an interlayer exciton comprising an electron in the $MoSe_2$ layer and hole in the WSe_2 layer is found to be stable and long-lived[3–6]. As shown in Fig. 1a, due to the spatial separation of electron and hole, the interlayer exciton carries a static, out-of-plane electric dipole moment that allows for the tuning of its energy by an external electric field (E). The orientation of this dipole is fixed by the ordering of $MoSe_2$ and WSe_2 layers and hence leads to a repulsive interaction between interlayer excitons.

This dipolar interaction is potentially interesting for inducing effective photon–photon interaction and making the heterobilayer a nonlinear optical medium for efficient photon switching applications[7–13]. Furthermore, repulsive dipolar interactions could also lead to exotic many-body states such as self-assembled dipolar crystals with a spin-valley degree of freedom at a critical density of excitons[14,15]. As a signature of nonlinearity, dipolar repulsion should result in an exciton density dependent blueshift of the emission energy with increasing incident power. While such a behaviour has been previously reported[16,17], a discernible shift of the emission energy, comparable to the linewidth, occurs only for a large number of excitons (≥400) and at the highest incident power.

To see a quantum nonlinearity where the presence of merely one additional exciton drastically modifies the optical response, the effective dipole–dipole interaction (U_{dd}) must be larger than the linewidth[10]. As the expected blueshift has a U_{dd} of roughly $1/r_{ex}^3$ where r_{ex} is the interexcitonic distance, localized interlayer excitons are good candidates for observing this effect. Localized excitons in monolayer WSe_2 have been shown to be single photon emitters with sharp linewidths[18–24] and can host a single charge and spin[25,26]. Very recently, localized interlayer excitons with sharp linewidths have been reported in van der Waals heterostructures[27]. As described in Fig. 1b, there is an on-site energy cost ($U_{dd}^{on-site}$) for creating two interlayer excitons within the same trap ($|IXX\rangle$) compared to a single excitation ($|IX\rangle$) with energy E_x. The situation is then reminiscent of dipole blockade in Rydberg atoms[28] albeit with a much smaller dipole moment and hence requiring tighter localization. In addition to increasing U_{dd}, localized interlayer excitons should also serve as quantum emitters consisting of a single dipole with tuneable emission energy in a perpendicular electric field.

To demonstrate dipole–dipole interactions in localized interlayer excitons, we fabricated a $MoSe_2/WSe_2$ heterobilayer encapsulated in hexagonal-BN layers with graphite top and bottom gates, as shown in Fig. 1c (see Methods). Figure 2a shows the low temperature (~4 K) photoluminescence (PL) spectra of our sample with emission from interlayer exciton clearly present at lower energy (~1.35 eV) compared to intralayer exciton peaks of $MoSe_2$ (WSe_2) at 1.65 eV (1.75 eV), consistent with previous studies[29]. Reflectance spectra of the heterobilayer region shown in Fig. 2b exhibits a redshift of intralayer exciton resonances compared to the monolayer regions as is expected from the interaction between the two monolayers[30]. The PL excitation (PLE) spectroscopy of the lower energy PL peaks shows resonances at excitation energies corresponding to $MoSe_2$ and WSe_2 excitons, as is expected for an exciton comprising charge carriers from both the monolayers (Fig. 2c).

To observe localized interlayer excitons, we switch to quasi-resonant excitation close to the $MoSe_2/WSe_2$ exciton and use low excitation power (see Methods). As Fig. 2d shows, we observe sharp, spatially localized peaks with linewidths as low as 110 μeV in the energy range of 1,260 to 1,330 meV (see Supplementary Figs. 1 and 2). Furthermore, these sharp emission peaks show spectral jittering that is characteristic of localized quantum emitters. Since the energy of the sharp peaks lies in the range of interlayer PL at higher power and because intralayer WSe_2- and $MoSe_2$-localized excitons typically exhibit energy higher than 1,560 meV (ref. [31]), we believe that such low-energy peaks should be related to the interlayer exciton. In addition, we perform PLE spectroscopy and find resonances at both $MoSe_2$ (~1,640 meV) and WSe_2 (~1,730 meV) excitons (Fig. 2e), similar to the case of interlayer excitons.

With electron and hole located in different layers due to the type-II band alignment, the interlayer exciton has an out-of-plane

[1]Department of Physics, Emory University, Atlanta, GA, USA. [2]These authors contributed equally: Weijie Li, Xin Lu. ✉e-mail: ajit.srivastava@emory.edu

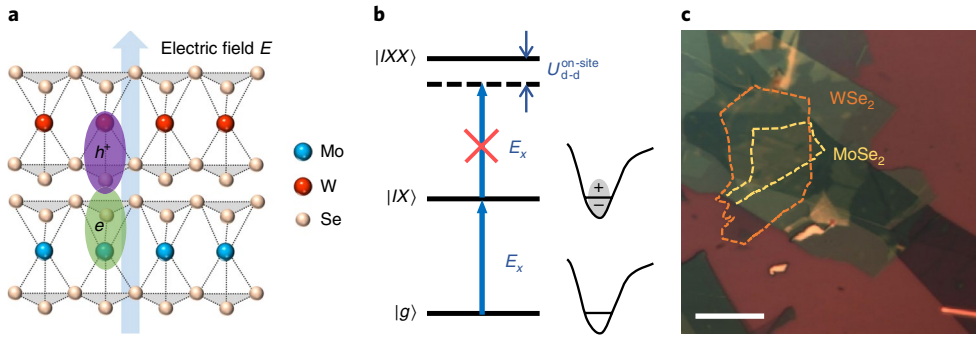

Fig. 1 | Interlayer exciton dipoles in $MoSe_2/WSe_2$ heterostructure. a, A schematic showing the interlayer exciton in $MoSe_2/WSe_2$ heterobilayer (blue sphere, Mo; red sphere, W; light-yellow sphere, Se; dashed lines show the covalent bonding between atoms; grey triangle shades indicate the Se planes) under an external electric field *E*. The direction of *E* is shown in the light-blue arrow. Due to the type-II band alignment, electron and hole are separated in $MoSe_2$ and WSe_2, respectively, forming a permanent out-of-plane dipole. Electron and hole wavefunctions are depicted as green and purple ovals, respectively. The dipole energy redshifts (blueshifts) when *E* is parallel (antiparallel) to the direction of dipole. **b**, Energy diagram of localized interlayer optical excitation in a potential well. $|g\rangle$, $|IX\rangle$ and $|IXX\rangle$ denote the ground, single- and double-occupancy states. The transition from $|g\rangle$ to $|IX\rangle$ (right, from empty to single occupancy) costs energy of E_x. In addition to E_x, the energy of biexciton (from $|IX\rangle$ to $|IXX\rangle$) is increased by an on-site dipole–dipole interaction $U_{dd}^{on-site}$. **c**, An optical image of a $MoSe_2/WSe_2$ heterobilayer with a graphite bottom gate. Monolayer WSe_2 ($MoSe_2$) is depicted with an orange (yellow) dashed line. The final device has graphite bottom and top gates with h-BN as dielectric on both sides. Scale bar, 10 μm.

permanent dipole and its energy should blueshift (redshift) by an amount of $\Delta U = |\mathbf{p} \cdot \Delta \mathbf{E} E|$ when *E* is antiparallel (parallel) to the the direction of dipole *p*. The dipole moment in our sample is 0.7 nm × *e* (where *e* is the elementary charge) and points from $MoSe_2$ (bottom layer) to WSe_2 (top layer)[5]. As shown in Fig. 2f, when the bottom gate voltage changes from −2 to +2 V (Δ*E* pointing up), the energy of interlayer exciton decreases by ~20 meV (see also Supplementary Fig. 3). Based on the calculated *E* using a capacitor model[32], we estimate the total thickness of hexagonal boron nitride to be 66 nm, consistent with the value of 80 nm estimated from the optical contrast (see Supplementary Fig. 4 and Supplementary Note 1). The observed tuning rate of ~400 meV nm V^{-1} in Fig. 2f is consistent with the analysis in ref. [16]. Meanwhile, a localized peak at 1,450 meV, possibly from $MoSe_2$, barely shifts with *E*. This is in agreement with the absence of out-of-plane dipole moment for an intralayer exciton. The *E* tuneability of sharp peaks unambiguously demonstrates that they arise from localized interlayer excitons. A desirable property of these emitters is that their energy can be tuned by more than 100 times their linewidth. Thus, we can conclude that localized interlayer excitons are excellent candidates to study dipolar interactions in 2D layered materials.

Having established that we have observed localized interlayer exciton with an out-of-plane dipole, we investigate their dipole–dipole interactions. To this end, we increase the excitation laser power to achieve larger density of excitons. Figure 3a is the time-trace PL emission of two peaks at ~1,360 and ~1,362 meV that show the same spectral jittering pattern, as highlighted by white arrows and dotted circles. This behaviour indicates that the two peaks belong to the same localizing potential well. A similar synchronized jittering feature is also observed in other localized interlayer excitons, with energy spacing between the two peaks varying from 1 to 5 meV (Fig. 3b and Supplementary Fig. 5). We notice that such synchronized spectral jittering is not shown by all the peaks in our collection spot. For example, the lowest-energy peak in Fig. 3b exhibits a different pattern. In localized intralayer excitons, a doublet peak structure showing similar synchronized jittering is seen and arises from the electron-hole exchange interaction, which causes a fine-structure splitting[23]. However, we can rule out the possibility of such fine-structure splitting, as the electron-hole exchange interaction is strongly quenched in interlayer exciton due to separation of carriers into distinct layers. Figure 3c shows that localized interlayer exciton and the blueshifted peak exhibiting the same *E*-tuning rate of ~310 meV nm^{-1} V^{-1} suggesting that they both carry a dipole moment. Thus, exciton complexes such as charged excitons and biexcitons could be the possible origin of the two-peak structure.

Excitation power dependence of emission intensity can be used to distinguish between charged excitons and biexcitons. Figure 3d shows PL spectra at different incident powers. At the lowest power, we only observe the red peak. As the power is increased, the blue peak starts to show up at intermediate power and becomes stronger than the red peak at higher power. This strongly indicates that the blue peak is possibly a biexciton. We thus assign the red and blue peaks the symbols IX and IXX, respectively. We further plot the integrated intensity of each emission peak as a function of excitation power, and fit the data with a power-law function, $I \propto P^{\alpha}$ (Fig. 3e and Supplementary Fig. 6). The red peak IX2 exhibits a power-law behaviour with $\alpha_X = 0.97 \pm 0.16$, and the blue peak IXX2 shows a super-linear power dependence with $\alpha_{XX} = 2.03 \pm 0.27$. The super-linear power dependence of the blue peak ($I \propto P^{2\alpha_X}$) is consistent with our assignment that the blue peak is a biexciton. To capture the saturation behaviour beyond the power-law regime, we use a three-level rate-equation model for exciton and biexciton occupation probabilities. We find good agreement of our data with the model, which further validates our assignment (see Supplementary Note 2 and Fig. 7).

While the biexciton in monolayer WSe_2 emits at a lower energy from PL spectroscopy because of a finite, positive binding energy[33], the energy of the interlayer biexciton state is raised up by U_{dd} due to dipolar repulsion (Fig. 4c). Emission from the biexciton is thus blueshifted with respect to the exciton (Fig. 3). In other words, the biexciton observed here is unlike a hydrogen molecule-like bound state but instead a double-occupancy state of the localizing trap. The motion of the two residing excitons gets correlated due to repulsive interactions. The different energy spacing (1–5 meV) between the exciton and biexciton indicates that the dipolar interaction varies among different localized interlayer excitons. As the dipole moment can be assumed to be constant given by the separation of 0.7 nm between the two monolayers, variation in U_{dd} must arise from difference in confinement lengths and consequently interexcitonic distances. To estimate the confinement length from U_{dd}, we assume that the interlayer excitons are confined in a harmonic trap with a width larger than the excitonic Bohr radius such that the dipoles

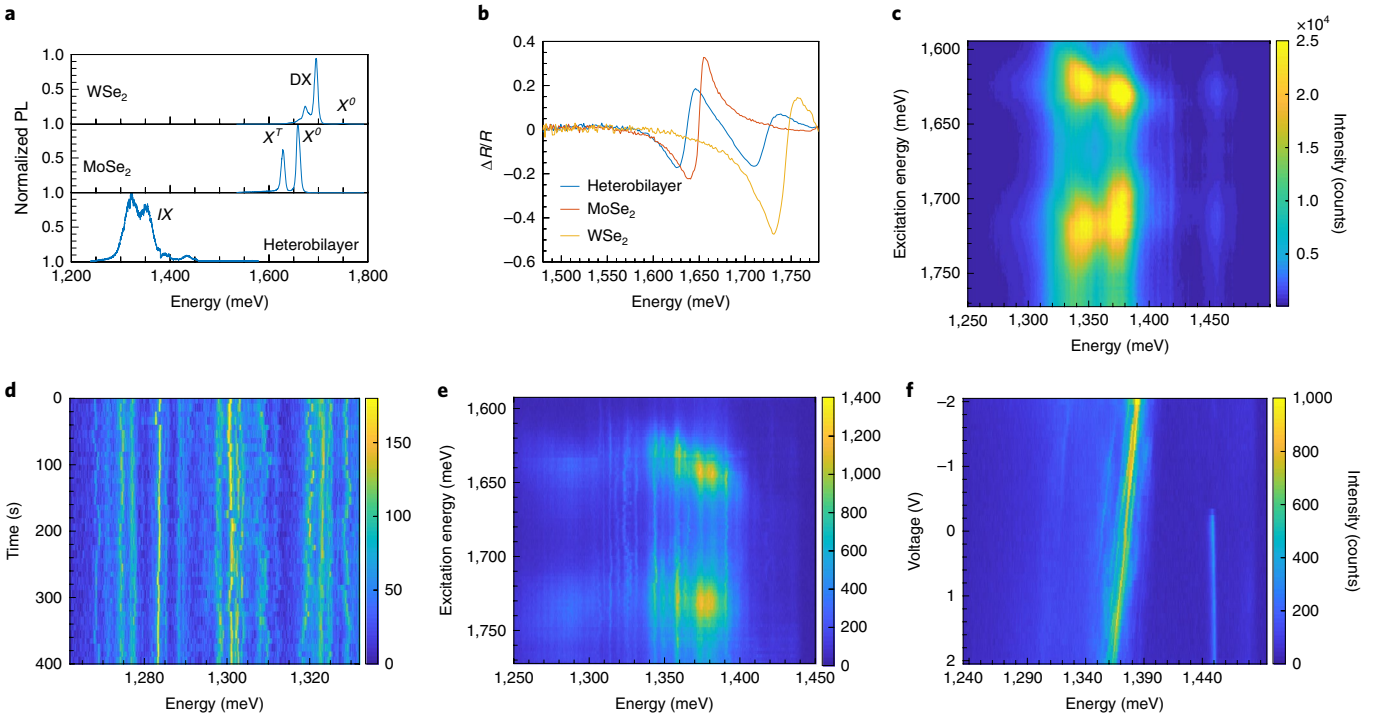

Fig. 2 | Excitons from $MoSe_2/WSe_2$ heterostructure at low temperature (~4 K). **a**, Normalized PL spectra. Top, emission from defect band (DX) dominates in WSe_2. Exciton X^0 is observed at ~1,750 meV. Middle, monolayer $MoSe_2$ shows two prominent peaks at 1,658 and 1,628 meV, corresponding to neutral exciton X^0 and trion X^T, respectively. Bottom, emission from interlayer exciton (IX) appears at lower energy (1,250–1,450 meV). **b**, Reflectance contrast $\Delta R/R$ spectra. $\Delta R/R = (R_{sample} - R_{substrate})/R_{substrate}$. The exciton resonances in monolayers (red, 1L $MoSe_2$; yellow, 1L WSe_2) are consistent with the observation from PL spectroscopy in **a**. Compared to monolayers, the intralayer excitons in heterobilayer (shown in blue) redshift and broaden. **c**, PLE spectroscopy of interlayer excitons. **d**, Time-trace PL emission of localized interlayer excitons. **e**, PLE of localized emitters. All the emitters show local resonances around ~1,640 meV ($MoSe_2$ resonance) and ~1,730 meV (WSe_2 resonance), consistent with the nature of interlayer excitons. **f**, *E* tuning of a localized interlayer exciton. As bottom gate voltage sweeps from −2 to +2 V, the localized interlayer exciton at ~1,380 meV exhibits a redshift of ~20 meV, confirming the existence of an out-of-plane dipole. As a comparison, the localized intralayer exciton at ~1,450 meV does not show *E* tuneability. Excitation laser is linearly polarized. Wavelength $\lambda = 633$ nm in **a**, $\lambda = 770$ nm in **d**, $\lambda = 758$ nm in **f**. Incident power $P = 2$, 5 and 20 μW from top to bottom in **a**, $P = 10$ nW in **d**, $P = 210$ nW in **f**.

can be treated as point particles without considering their internal structure, whereas treating the excitons as point particles is strictly valid only when inter-dipole distance is much larger than the Bohr radius; as shown next, our simple model gives good qualitative agreement with the data.

When the trap is loaded with an additional exciton, the centre-of-mass wavefunction of each exciton is squeezed to avoid overlap and lower the dipolar repulsion. The modified centre of mass wavefunction of each exciton is no longer that of the ground state but has weight from higher energy excited states. This results in the increase of kinetic energy of the two-particle system. The interexcitonic distance can then be calculated by minimizing the total energy that includes $U_{dd} = p^2/(\epsilon_r r_{ex}^3)$. For an energy difference of 2 meV between the exciton ($|IX\rangle \rightarrow |g\rangle$) and biexciton ($|IXX\rangle \rightarrow |IX\rangle$) emission peaks, we obtain an inter-dipole distance of ~7 nm, which is larger than the Bohr radius (~2 nm) (see Supplementary Note 3 and Supplementary Fig. 8). We remark that one of the peaks from another localized interlayer exciton (IXXX5) shows power dependence with $I \propto P^{3\alpha}$, and possibly corresponds to a triexciton (see Supplementary Figs. 9 and 10). Indeed, the energy difference of this peak with respect to the biexciton peak agrees well with a regular arrangement of three excitons, which reduces dipolar repulsion (see Supplementary Notes 4 and 5 and Supplementary Fig. 11)[34]. Finally, with higher incident powers, new peaks appear at systematically higher energies compared to the biexciton peak (see Supplementary Information and Supplementary Fig. 12).

It is very probable that, like their intralayer counterparts, interlayer excitons also get trapped in shallow potentials due to strain or defect potential on a length scale larger than the interlayer exciton Bohr radius[23]. Another possible cause of trapping is moiré potential arising from a finite twist between the monolayers, which is ~2–6° in our samples. Figure 4a,b shows that the IX2 and IXX2 have the same *g*-factor of ~6.5 (see Supplementary Fig. 13 for IX5 group), which is consistent with the emitters reported in ref. [27] for the case of near 0° alignment. Assuming a moiré period dependence of 19 nm per degree[35], the moiré period for our case should be ~3–9 nm, which is indeed consistent with our estimate of interexcitonic distance. However, lattice relaxation often modifies the pristine moiré pattern to larger domain sizes[36]. The polarization of PL from localized interlayer excitons is insensitive to the helicity of the excitation laser, unlike in the case of emitters reported in ref. [27], and has a substantial linearly polarized component (see Supplementary, Fig. 14). This is probably because of the anisotropic strain in our heterostructures that reduces the symmetry of a pristine moiré pattern.

In addition to having an out-of-plane dipole, interlayer excitons also possess a spin-valley degree of freedom. Much like the intralayer excitons, the interlayer excitons comprise electron and hole in $\pm K$ valleys, $X_{\pm}$, couple to circularly polarized light with opposite helicity ($\sigma^{\pm}$) following the optical selection rule[37,38]. In addition, depending on the species of biexciton that is, same valley (X_+X_+ or X_-X_-) or opposite valley (X_+X_-) IXXs should be affected by exciton–exciton exchange interaction, U_{ex}, in addition to U_{dd}.

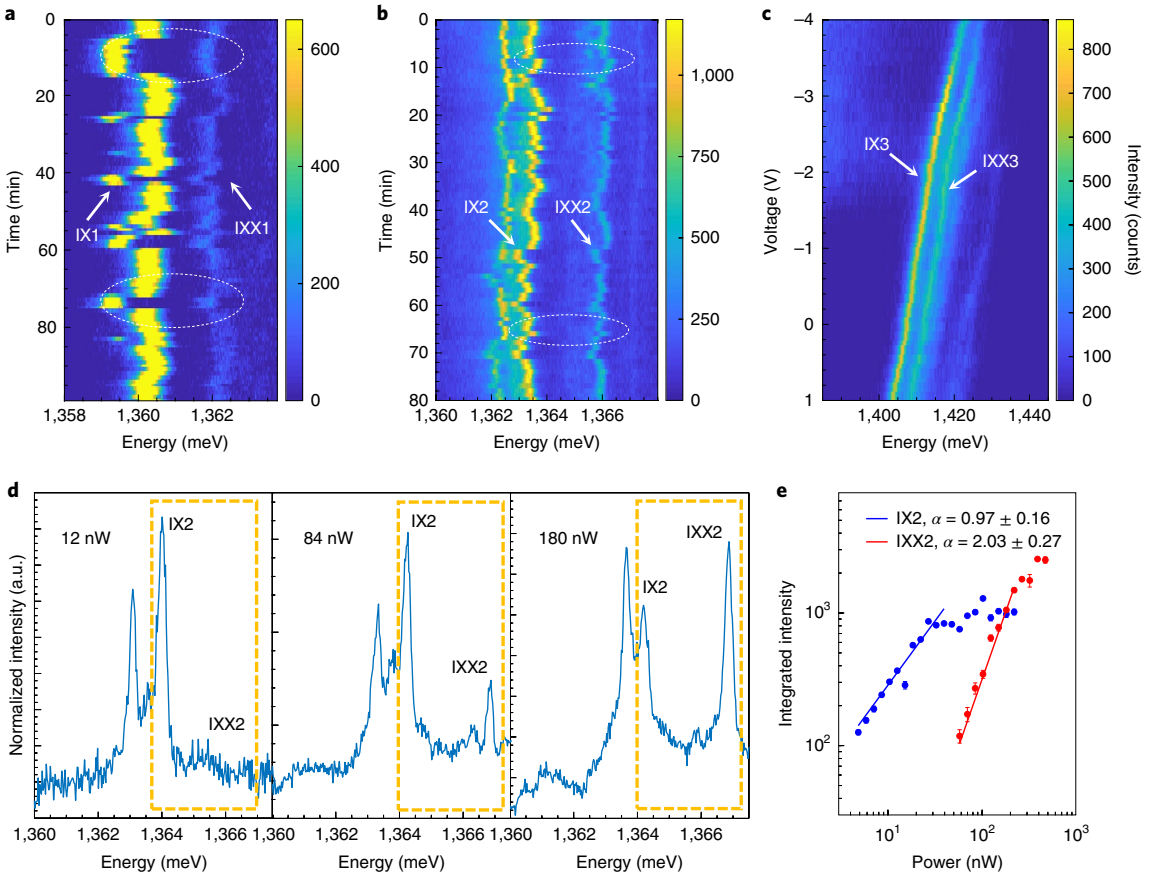

Fig. 3 | Signatures of localized interlayer biexcitons. a,**b**, Time-trace of PL emission of localized interlayer excitons and biexcitons. White arrows and dotted circles highlight the same spectral jittering patterns from IX1–IXX1 (**a**) and IX2–IXX2 (**b**), indicating that they originate from the same localized potential, respectively. **c**, *E* tuning of interlayer exciton IX3 and biexciton IXX3. The two peaks exhibit the same tuning rate of ~310 meV nm^{-1} V^{-1}. **d**, PL spectra of IX2–IXX2 (highlighted in yellow dashed rectangles) under different excitation powers, 12 nW (left), 84 nW (middle) and 180 nW (right). Only exciton IX2 shows up at low power (12 nW). Biexciton IXX2 appears at intermediate power (84 nW) and dominates at high power (180 nW). a.u., arbitrary units. **e**, Integrated intensity of emission peaks as a function of excitation power for IX2–IXX2. The experimental data were extracted after fitting the PL spectra with a Lorentzian function. The fitting of power dependence was done with a power-law function, $I \propto P^{\alpha}\alpha(\mathrm{IXX2}) \approx 2\alpha(\mathrm{IX2})$, suggesting that IXX2 is a biexciton. Error bars for both extracted intensities and power-law scaling coefficients arise from fitting. The excitation laser is linearly polarized. Wavelength $\lambda = 745$ nm in **a**,**b**,**d**,**e**, $\lambda = 758$ nm in **c**. Incident power $P = 20$ nW in **a**, $P = 250$ nW in **b** and $P = 4\,\mu$W in **c**.

The wavefunction of the lowest-energy two-exciton state is anti-symmetric in the spatial coordinates to minimize the dipolar repulsion. The bosonic nature of the exciton then implies that the singlet arrangement of spin-valley or the opposite valley biexciton X_+X_- has lower energy whereas the same valley excitons $X_\pm X_\pm$ have energy further increased by U_{ex} (Fig. 4c).

Next, we analyse the spin-valley structure of the biexciton peaks by performing polarization-resolved measurements under magnetic field (B). As we only observe one extra peak appearing with larger power, we tentatively suppose this peak is the lower energy X_+X_- biexciton rather than the degenerate X_+X_+ and X_-X_-. U_{ex} needs to be overcome for the observation of X_+X_+ and X_-X_- while emission typically arises only from the lowest-energy state due to thermalization at low temperatures. The degeneracy of X_+X_+ and X_-X_-, as well as X_+ and X_-, is lifted under finite magnetic field, B (dashed line in Fig. 4c). As illustrated in Fig. 4c, the degeneracy lifting of exciton states causes the PL emission from X_+X_+/X_-X_- to split into two peaks while X_+X_- state is hardly affected under B. Copolarized emission is expected with all red (blue) peaks emitting σ^+ (σ^-) polarized light, as shown in the schematic of Fig. 4c. From polarization-resolved PL measurements (Fig. 4d,e), we observe that both red (IXX2$_-$) and blue peaks (IXX2$_+$) of IXX2 are copolarized with the corresponding red (IX2$_-$) and blue (IX2$_+$) peaks of IX, consistent with the energy diagram in Fig. 4c (see Supplementary Figs. 15 and 16 for detailed B dependence).

To further confirm that the biexciton peak corresponds to a spin-valley singlet configuration, X_+X_-, we analyse the intensity of emission of the two circularly polarized components. In principle, the intensity of X_+X_- ($I_{X_+X_-}$) should be proportional to the product $I_{X_+}I_{X_-}$. Likewise, $I_{X_+X_+}$ ($I_{X_-X_-}$) would be higher if $I_{X_+}I_{X_+}$ ($I_{X_-}I_{X_-}$) is larger. We use excitation polarization to control the degree of circular polarization (DCP) of the exciton under finite B, such that the relative intensity between X_+ and X_- is modulated while keeping the total intensity unchanged. DCP is obtained by calculating $(I_{\sigma^+} - I_{\sigma^-})/(I_{\sigma^+} + I_{\sigma^-})$, where a positive (negative) value means the peak is σ^+ (σ^-) polarized. Because the exciton is less circularly polarized with σ^- pumping at -0.5 T, we expect IXX2 to be stronger if it is X_+X_-. A histogram based on more than 50 polarization-resolved spectra for each polarization confirms our analysis (Fig. 4f). The mean integrated intensity from σ^- excitation is ~7,000, and that from σ^+ excitation is only ~5,700. To further support our assignment, we calculate the ratio of $I_{XX}/I_{X_+}I_{X_-}$, $I_{XX}/I_{X_+}I_{X_+}$ and $I_{XX}/I_{X_-}I_{X_-}$ (Supplementary Table I). For X_+X_- biexciton, I_{XX} should be proportional to $I_{X_+}I_{X_-}$, regardless of the exciton polarization.

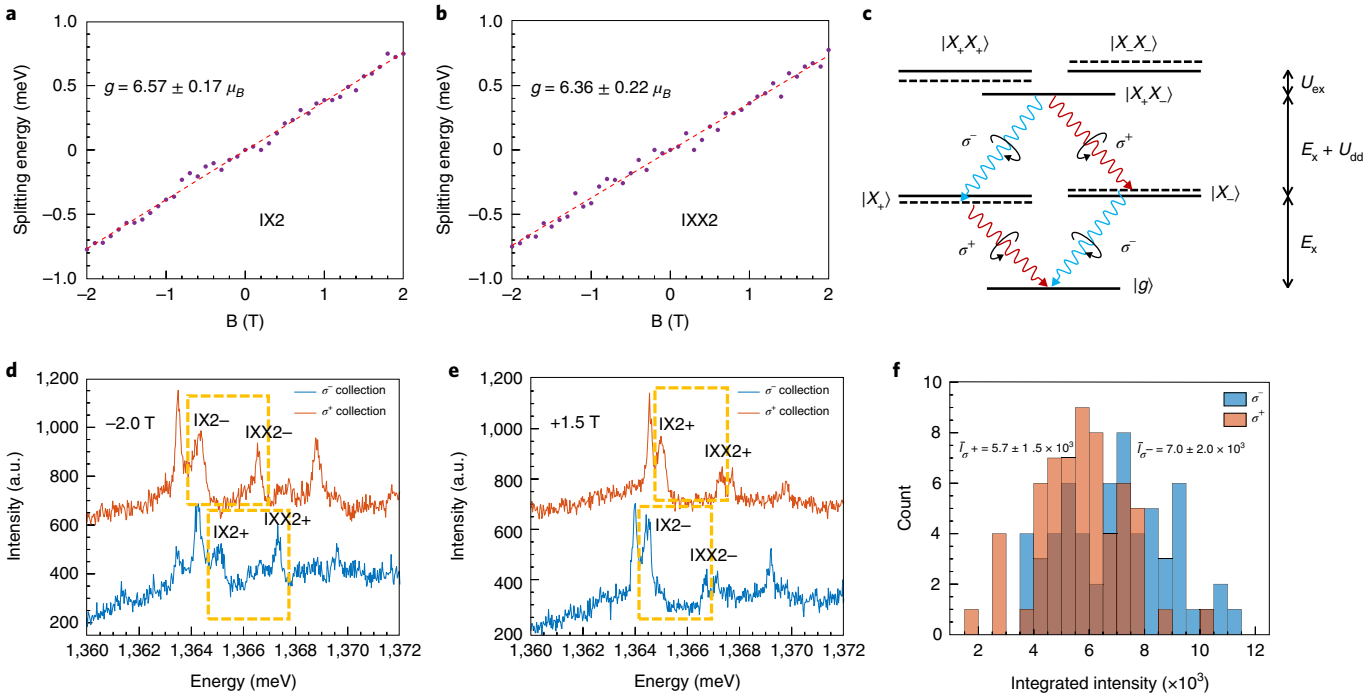

Fig. 4 | Spin-valley structure of localized interlayer excitons and biexcitons under magnetic field. a,**b**, *B*-dependent splitting energies of IX2 (**a**) and IXX2 (**b**). Exciton and biexciton exhibit the same value of *g*-factor, ~6.5 (μ_B is the Bohr magneton). **c**, Optical selection rule of IX and IXX under *B*. $|g\rangle$ represents the ground state. $|X_+\rangle$ and $|X_-\rangle$ are referred to excitons from opposite valleys, and the two states are degenerate at zero *B* (solid lines). E_x denotes the energy from $|g\rangle$ to $|X_+\rangle$ or $|X_-\rangle$ state. The transition from exciton to biexciton states needs to overcome dipolar repulsion U_{dd} in addition to E_x. $|X_+X_-\rangle$, $|X_+X_+\rangle$ and $|X_-X_-\rangle$ are biexciton states. The doubly degenerate $|X_+X_+\rangle$ and $|X_-X_-\rangle$ states are higher than $|X_+X_-\rangle$ because of the exciton–exciton exchange interaction U_{ex}. Degeneracy lifting of $|X_+\rangle$ and $|X_-\rangle$ under finite *B* (dashed lines) leads to the splitting of $|X_+X_-\rangle$ emission. Red (blue) peaks of exciton and biexciton are both σ^+ (σ^-) polarized. Degeneracy of $|X_+X_+\rangle$ and $|X_-X_-\rangle$ is also lifted under *B*. **d**,**e**, Polarization-resolved PL spectra of IX2 and IXX2 (highlighted in yellow dashed rectangles) at −2.0 T (**d**) and +1.5 T (**e**). IX2− (IX2+) and IXX2− (IXX2+) denote red (blue) split peaks of IX2 and IXX2 under finite *B*. σ^- (σ^+) collection is shown in blue (red). Polarization of the biexciton peaks follows that of the exciton. Red traces are vertically offset for clarity. **f**, Histogram of biexciton intensity under σ^+ (red) and σ^- (blue) excitation configurations at −0.5 T where $\bar{I}$ is the average integrated intensity. Biexciton is stronger under σ^- excitation, consistent with the fact that the DCP of exciton is lower when being excited with σ^- polarized light (see Supplementary Information and Supplementary Fig. 15). Excitation wavelength $\lambda = 745$ nm in panels **a**,**b**,**d**–**f**. Incident power $P = 250$ nW (linearly polarized) in **b**–**e**, $P = 150$ nW (circularly polarized) in **f**.

However, such a proportionality does not hold for $I_{XX}/I_{X_+}I_{X_+}$ and $I_{XX}/I_{X_-}I_{X_-}$, confirming our assumption that the biexciton state is a spin-valley singlet. We characterize the difference of ratio (R) between σ^+ and σ^- excitations by calculating $2(R(\sigma^+) - R(\sigma^-))/(R(\sigma^+) + R(\sigma^-))$. The difference of ratio is one order of magnitude smaller for $I_{XX}/I_{X_+}I_{X_-}$ compared to that of $I_{XX}/I_{X_+}I_{X_+}$ and $I_{XX}/I_{X_-}I_{X_-}$ (Supplementary Table I), which is consistent with our assignment that IXX2 is a X_+X_- biexciton.

Although expected, single photon emission from localized interlayer excitons was not demonstrated here because of their weak emission intensity (see, however, Supplementary Note 6). Future experiments incorporating localized interlayer excitons in plasmonic nanocavities should be able to enhance the emission rate, as was recently demonstrated for monolayer quantum emitters[39–41]. Thus, localized interlayer excitons with finite dipole moment are potentially quantum emitters with *E*-field-tuneable energy over a wide range. Moreover, their biexciton cascade emission (Fig. 4c) is devoid of the fine-structure splitting due to absence of electron-hole exchange interaction that limits the entanglement fidelity of the emitted photon pair in intralayer excitons[33,42]. While the emission rate of our localized interlayer excitons (20 counts per s, see Methods) is slightly larger than the previously reported values[27], it is still too weak to detect entangled photons in a photon coincidence measurement. Another possibility is to employ recently observed layer-hybridized interlayer excitons in van der Waals heterobilayers where one of the charge carriers is delocalized in both layers, thereby increasing the oscillator strength[43,44].

In addition, due to their static dipole moment, electrostatic confinement seems to be the natural way to realize an array of quantum emitters with the on-site dipole repulsion leading to the Mott phase of the Bose–Hubbard model[35,37]. Another interesting possibility is to confine many dipolar excitons in a larger trap (tens of nm). With increasing exciton density, a crystallization phase transition to one- or two-dimensional dipolar crystal might occur, which could be probed through their phonon modes[14]. A dipolar crystal of an interlayer excitonic condensate might give rise to more exotic many-body states such as supersolids while the internal spin-valley degree of freedom could lead to magnetic instabilities and frustration.

Note added in proof: Recently, a manuscript appeared reporting similar results on interlayer excitons trapped in a van der Waals heterobilayer[45].

Online content

Any methods, additional references, Nature Research reporting summaries, source data, extended data, supplementary information, acknowledgements, peer review information; details of author contributions and competing interests; and statements of data and code availability are available at https://doi.org/10.1038/s41563-020-0661-4.

Received: 18 October 2019; Accepted: 10 March 2020;
Published online: 13 April 2020

References

1. Chernikov, A. et al. Exciton binding energy and non-hydrogenic rydberg series in monolayer WS_2. *Phys. Rev. Lett.* **113**, 076802 (2014).
2. He, K. et al. Tightly bound excitons in monolayer WSe_2. *Phys. Rev. Lett.* **113**, 026803 (2014).
3. Rivera, P. et al. Observation of long-lived interlayer excitons in monolayer $MoSe_2$–WSe_2 heterostructures. *Nat. Commun.* **6**, 6242 (2015).
4. Tran, K. et al. Evidence for moiré excitons in van der Waals heterostructures. *Nature* **567**, 71–75 (2019).
5. Rivera, P. et al. Valley-polarized exciton dynamics in a 2D semiconductor heterostructure. *Science* **351**, 688–691 (2016).
6. Fogler, M. M., Butov, L. V. & Novoselov, K. S. High-temperature superfluidity with indirect excitons in van der Waals heterostructures. *Nat. Commun.* **5**, 4555 (2014).
7. Birnbaum, K. M. et al. Photon blockade in an optical cavity with one trapped atom. *Nature* **436**, 87–90 (2005).
8. Faraon, A. et al. Coherent generation of non-classical light on a chip via photon-induced tunnelling and blockade. *Nat. Phys.* **4**, 859–863 (2008).
9. Imamoğlu, A., Schmidt, H., Woods, G. & Deutsch, M. Strongly interacting photons in a nonlinear cavity. *Phys. Rev. Lett.* **79**, 1467–1470 (1997).
10. Chang, D. E., Vuletić, V. & Lukin, M. D. Quantum nonlinear optics—photon by photon. *Nat. Photon.* **8**, 685–694 (2014).
11. Carusotto, I. & Ciuti, C. Quantum fluids of light. *Rev. Mod. Phys.* **85**, 299–366 (2013).
12. Chang, D. et al. Crystallization of strongly interacting photons in a nonlinear optical fibre. *Nat. Phys.* **4**, 884–889 (2008).
13. Lukin, M. et al. Dipole blockade and quantum information processing in mesoscopic atomic ensembles. *Phys. Rev. Lett.* **87**, 037901 (2001).
14. Rabl, P. & Zoller, P. Molecular dipolar crystals as high-fidelity quantum memory for hybrid quantum computing. *Phys. Rev. A.* **76**, 042308 (2007).
15. Lahaye, T., Menotti, C., Santos, L., Lewenstein, M. & Pfau, T. The physics of dipolar bosonic quantum gases. *Rep. Prog. Phys.* **72**, 126401 (2009).
16. Ciarrocchi, A. et al. Polarization switching and electrical control of interlayer excitons in two-dimensional van der Waals heterostructures. *Nat. Photon.* **13**, 131–136 (2019).
17. Nagler, P. et al. Interlayer exciton dynamics in a dichalcogenide monolayer heterostructure. *2D Mater.* **4**, 025112 (2017).
18. Srivastava, A. et al. Optically active quantum dots in monolayer WSe_2. *Nat. Nanotechnol.* **10**, 491–496 (2015).
19. Koperski, M. et al. Single photon emitters in exfoliated WSe_2 structures. *Nat. Nanotechnol.* **10**, 503–506 (2015).
20. Chakraborty, C., Kinnischtzke, L., Goodfellow, K. M., Beams, R. & Vamivakas, A. N. Voltage-controlled quantum light from an atomically thin semiconductor. *Nat. Nanotechnol.* **10**, 507–511 (2015).
21. He, Y.-M. et al. Single quantum emitters in monolayer semiconductors. *Nat. Nanotechnol.* **10**, 497–502 (2015).
22. Tonndorf, P. et al. Single-photon emission from localized excitons in an atomically thin semiconductor. *Optica* **2**, 347–352 (2015).
23. Atatüre, M., Englund, D., Vamivakas, N., Lee, S.-Y. & Wrachtrup, J. Material platforms for spin-based photonic quantum technologies. *Nat. Rev. Mater.* **3**, 38–51 (2018).
24. Aharonovich, I., Englund, D. & Toth, M. Solid-state single-photon emitters. *Nat. Photon.* **10**, 631–641 (2016).
25. Lu, X. et al. Optical initialization of a single spin-valley in charged WSe_2 quantum dots. *Nat. Nanotechnol.* **14**, 426–431 (2019).
26. Brotons-Gisbert, M. et al. Coulomb blockade in an atomically thin quantum dot coupled to a tunable fermi reservoir. *Nat. Nanotechnol.* **14**, 442–446 (2019).
27. Seyler, K. L. et al. Signatures of moiré-trapped valley excitons in $MoSe_2$/WSe_2 heterobilayers. *Nature* **567**, 66–70 (2019).
28. Saffman, M., Walker, T. G. & Mølmer, K. Quantum information with Rydberg atoms. *Rev. Mod. Phys.* **82**, 2313–2363 (2010).
29. Rivera, P. et al. Interlayer valley excitons in heterobilayers of transition metal dichalcogenides. *Nat. Nanotechnol.* **13**, 1004–1015 (2018).
30. Schaibley, J. R. et al. Directional interlayer spin-valley transfer in two-dimensional heterostructures. *Nat. Commun.* **7**, 13747 (2016).
31. Branny, A. et al. Discrete quantum dot like emitters in monolayer $MoSe_2$: spatial mapping, magneto-optics, and charge tuning. *Appl. Phys. Lett.* **108**, 142101 (2016).
32. Wang, Z., Chiu, Y.-H., Honz, K., Mak, K. F. & Shan, J. Electrical tuning of interlayer exciton gases in WSe_2 bilayers. *Nano Lett.* **18**, 137–143 (2018).
33. He, Y.-M. et al. Cascaded emission of single photons from the biexciton in monolayered WSe_2. *Nat. Commun.* **7**, 13409 (2016).
34. Schinner, G. J. et al. Confinement and interaction of single indirect excitons in a voltage-controlled trap formed inside double InGaAs quantum wells. *Phys. Rev. Lett.* **110**, 127403 (2013).
35. Wu, F., Lovorn, T., Tutuc, E. & MacDonald, A. H. Hubbard model physics in transition metal dichalcogenide moiré bands. *Phys. Rev. Lett.* **121**, 026402 (2018).
36. Alden, J. S. et al. Strain solitons and topological defects in bilayer graphene. *Proc. Natl Acad. Sci. USA* **110**, 11256–11260 (2013).
37. Yu, H., Liu, G.-B., Tang, J., Xu, X. & Yao, W. Moiré excitons: from programmable quantum emitter arrays to spin-orbit–coupled artificial lattices. *Sci. Adv.* **3**, e1701696 (2017).
38. Wu, F., Lovorn, T. & MacDonald, A. Theory of optical absorption by interlayer excitons in transition metal dichalcogenide heterobilayers. *Phys. Rev. B.* **97**, 035306 (2018).
39. Luo, Y. et al. Deterministic coupling of site-controlled quantum emitters in monolayer WSe_2 to plasmonic nanocavities. *Nat. Nanotechnol.* **13**, 1137–1142 (2018).
40. Tripathi, L. N. et al. Spontaneous emission enhancement in strain-induced WSe_2 monolayer-based quantum light sources on metallic surfaces. *ACS Photonics* **5**, 1919–1926 (2018).
41. Cai, T. et al. Radiative enhancement of single quantum emitters in WSe_2 monolayers using site-controlled metallic nanopillars. *ACS Photonics* **5**, 3466–3471 (2018).
42. Huber, D. et al. Strain-tunable GaAs quantum dot: a nearly dephasing-free source of entangled photon pairs on demand. *Phys. Rev. Lett.* **121**, 033902 (2018).
43. Alexeev, E. M. et al. Resonantly hybridized excitons in moiré superlattices in van der Waals heterostructures. *Nature* **567**, 81–86 (2019).
44. Hsu, W.-T. et al. Tailoring excitonic states of van der Waals bilayers through stacking configuration, band alignment, and valley spin. *Sci. Adv.* **5**, eaax7407 (2019).
45. Kremser, M. et al. Discrete interactions between a few interlayer excitons trapped at a $MoSe_2$-WSe_2 heterointerface. Preprint at https://arxiv.org/abs/1907.08815 (2019).

Methods

Sample fabrication. We use electron beam lithography and thermal evaporator to fabricate the pillar arrays (5 nm Cr/85 nm Au) or electrical contacts (5 nm Cr/55 nm Au) on 300 nm SiO_2/Si substrates. A thin layer of SiO_2 (3 nm) is subsequently deposited on pillars by using atomic layer deposition as the spacer. We transfer the mechanically exfoliated samples by polydimethylsiloxane-based dry transfer method on the as-patterned pillars/electrical contacts, with monolayer WSe_2 (HQ graphene) on top of monolayer $MoSe_2$ (HQ graphene). The sample with electrical contacts is encapsulated between two hexagonal boron nitride (HQ graphene) layers. Graphite layers are used as the bottom gate and top gates. After the stacking of top $MoSe_2$, the sample is annealed in 5% H_2/95% N_2 at 125 °C for 2 h.

PL spectroscopy. We use two home-built, low temperature (~4 K) microscope setups for PL measurements. The sample is loaded into a closed-cycle cryostat (AttoDry 800) with electrical connection and subsequently into another cryostat (BlueFors cryogenics) with magnetic field from −8 to +8 T. A piezoelectric controller (Attocube systems) is used to position the sample. Emission is collected using an achromatic lens (numerical aperture, 0.42 for AttoDry 800 and numerical aperture of 0.63 for BlueFors cryogenics) and directed to a high-resolution (focal length, 500 mm for AttoDry 800 and 750 mm for BlueFors cryogenics) spectrometer (Princeton Instrument HR-500 for AttoDry 800 and Princeton Instruments SP-2750i for BlueFors cryogenics) where it is dispersed by a 1,200 grooves per mm or 300 grooves per mm grating (both blazed at 750 nm). A charge coupled device (Princeton Instrument PIXIS-400 CCD for AttoDry 800 and PyLoN CCD for BlueFors cryogenics) is used as a detector. The excitation laser is a mode-hop-free tuneable continuous-wave Ti:Sapphire laser (MSquared Lasers) with resolution of 0.1 pm or a HeNe laser (632.8 nm). The Ti:Sapphire (HeNe) laser has a spot size of ~1 μm (~2 μm). The polarization of incident laser is controlled by using a polarizer together with a liquid crystal variable retarder. Polarization-resolved measurements are performed by using a $\lambda/4$ waveplate (achromatic, 690–1,200 nm) placed before a Wollaston prism. Circularly polarized emission is converted into linearly polarized light through the $\lambda/4$ waveplate. The s and p components of linear polarized light are then displaced by the Wollaston prism. Another achromatic $\lambda/4$ waveplate is placed after the Wollaston prism to convert the linearly polarized light into a circularly polarized signal, to avoid the sensitivity to the grating efficiency. In all measurements, the magnetic field is applied perpendicular to the plane of the sample and the voltage is applied to the graphite gates with a Keithley 2400 sourcemeter.

Data availability

The data represented in Figs. 2–4 are provided with the paper as source data. All other data that support results in this article are available from the corresponding author on reasonable request.

Acknowledgements

We thank A. Imamoğlu and M. Kroner for many enlightening discussions. We also thank R. Lemasters and H. Harutyunyan for assistance with atomic layer deposition. A.S. acknowledges support from the National Science Foundation through the EFRI programme, grant no. EFMA-1741691 and National Science Foundation DMR award no. 1905809.

Author contributions

A.S., W.L., X.L. and S.D. conceived the project. W.L., X.L., S.D. and L.D. carried out the measurements. W.L. performed the theoretical calculations. X.L., S.D. and L.D. prepared the samples. A.S. supervised the project. All authors were involved in analysis of the experimental data and contributed extensively to this work.

Competing interests

The authors declare no competing interests.

Additional information

Supplementary information is available for this paper at https://doi.org/10.1038/s41563-020-0661-4.

Correspondence and requests for materials should be addressed to A.S.

Reprints and permissions information is available at www.nature.com/reprints.